Dual-atom Fe(II,III)N$_2$(μ$_2$-N)$_2$Cu(I,II)N moieties anchored on porous N-doped carbon driving high-efficiency oxygen reduction reaction

Mengyuan Xu [a,1], Lilong Zhang [c,1], Xiao Liang [a], Hong Xiao [a], Huifeng Zhuang [a], Fanchao Zhang [a], Tengfei Zhang [a], Pinyu Han [a], Wenjing Dai [a], Fan Gao [a], Jian Zhang [c,*], Lirong Zheng [b,*], Qiuming Gao [a,*]

[a] *Key Laboratory of Bio-inspired Smart Interfacial Science and Technology of Ministry of Education, Beijing Advanced Innovation Center for Biomedical Engineering, School of Chemistry, Beihang University, Beijing 100191, PR China*
[b] *Beijing Synchrotron Radiation Facility, Institute of High Energy Physics, Chinese Academy of Sciences, Beijing 100049, PR China*
[c] *Key Laboratory of Material Chemistry for Energy Conversion and Storage, Ministry of Education, Hubei Key Laboratory of Material Chemistry and Service Failure, School of Chemistry and Chemical Engineering, Huazhong University of Science and Technology, Wuhan, Hubei 430074, PR China*

ARTICLE INFO

ABSTRACT

Atomically distributed iron electrocatalyst is valid for oxygen reduction reaction (ORR). However, accurate regulation of the structure improving its intrinsic activity is a challenge. Herein, a dual-atom catalyst FeCu-NC with atomically distributed Fe and Cu co-anchored on porous N-doped carbon is obtained. The FeN$_4$ and CuN$_3$ couple sites bridged by two nitrogen atoms, exist as Fe(II,III)N$_2$(μ$_2$-N)$_2$Cu(I,II)N moieties with the metal distance of ~2.5 Å in the structure of FeCu-NC. The synergistic effect of Fe and Cu dual-atom reducing the dissociation energy of *OOH intermediate, allows an optimized 4e$^-$ ORR reaction pathway. The FeCu-NC exhibits high-efficiency ORR activity with the half-wave potential ($E_{1/2}$) of 0.889 V (vs RHE) and outstanding stability without obvious decay for the $E_{1/2}$ after 10,000 cycles. The FeCu-NC based Zn-air battery presents large specific capacity of 795 mAh g^{-1} and energy density of 998 Wh kg^{-1} as well as high charge-discharge cycling stability superior to the Pt/C.

1. Introduction

Zn-air battery possessing of high theoretical energy density (1086 Wh kg^{-1}), low manufacturing cost, non-toxicity and intrinsic safety, is attracting widespread attention as the cleaner and sustainable energy storage system [1–3]. During the discharging process, oxygen reduction reaction (ORR) involving multiple electron adsorption and desorption processes occurred on the air electrode [4]. Nevertheless, the high energy barriers and sluggish processes of ORR limit the practical utilization of Zn-air battery [5–7]. Even though platinum-based catalysts are effective for the ORR, the high cost, limited reserves and poor durability sternly restrict the large-scale application [8,9]. Transition metal-based catalysts with the unfilled d-orbitals are beneficial for the ORR process, becoming low-cost substitutes for precious metal catalysts [10]. As to bulk catalysts only a small fraction of the surface atoms is involved in the catalytic reaction [11]. The atomic utilization was being maximized by increasing the specific surface area and volume ratio of the catalyst via continuously reducing the particle size [12,13]. Single-atom catalysts (SACs) with the maximum atoms utilization and fully exposed active sites are the pursuit of efficient ORR [14–16].

Recently, Fe SACs possessing of well-defined structures, comparable or even superior ORR electrocatalytic activity to the commercial Pt/C catalyst were reported [17]. According to the ORR volcano plot curve [18,19], the adsorption energy of oxygen intermediates on the FeN$_4$ moieties is strong with the location on the left side of the curve, indicating that the potential rate-determining step (RDS) is the desorption of the *OH intermediate [20]. Introducing other transitional metal atoms in the Fe SACs could effectively optimize the FeN$_4$ electronic structure with charge redistribution and adjust d-band center, resulting in the enhanced ORR electrocatalytic activity, such as dual single-atom catalysts (DACs) of Fe-Co[21], Fe-Ni [22], Fe-Zn and Fe-Mn [23], etc.[24]. Noteworthy, Cu is a non-precious metal element second only to the

---

precious metals on the ORR volcano plot curve [18]. The high redox potential and d-orbital electron density of Cu element could lead to weak O-O bonds [25]. The multiple valence states, i.e., Cu^0, Cu^+ and Cu^{2+}, exhibited rich multielectron redox properties, which are possibly favorable for redistribution of charge around the FeN_4 active sites [26, 27]. Thus, introducing atomically dispersed Cu atoms into Fe SACs may be an effective strategy to improve the ORR activity by adjusting the charge around the FeN_4 active sites and further optimizing the adsorption ability of Fe active centers for oxygen species.

Herein, a novel kind of atomically dispersed Fe and Cu dual atoms co-anchored on nitrogen-doped carbonaceous catalyst (named as FeCu-

NC) was synthesized by a facile pyrolysis technique using ZIF-8-FePc/CuPc as the precursor. The introduced CuN_3 moieties can effectively change the charge distribution around the FeN_4 electrocatalytic active sites. As a result, the FeCu-NC DACs with $Fe(II,III)N_2(\mu_2\text{-}N)_2Cu(I,II)N$ moieties exhibited a high-efficiency ORR electrocatalytic activity and outstanding stability. First-principle density functional theory (DFT) calculations corroborated that the CuN_3 moieties optimized the ORR path over the FeN_4 active sites, whose dissociation energy for *OOH intermediate was obviously reduced caused by the synergistic effect of Fe-Cu dual atoms, facilitating the whole ORR process. The self-assembly Zn-air battery based on the FeCu-NC DAC presented large specific
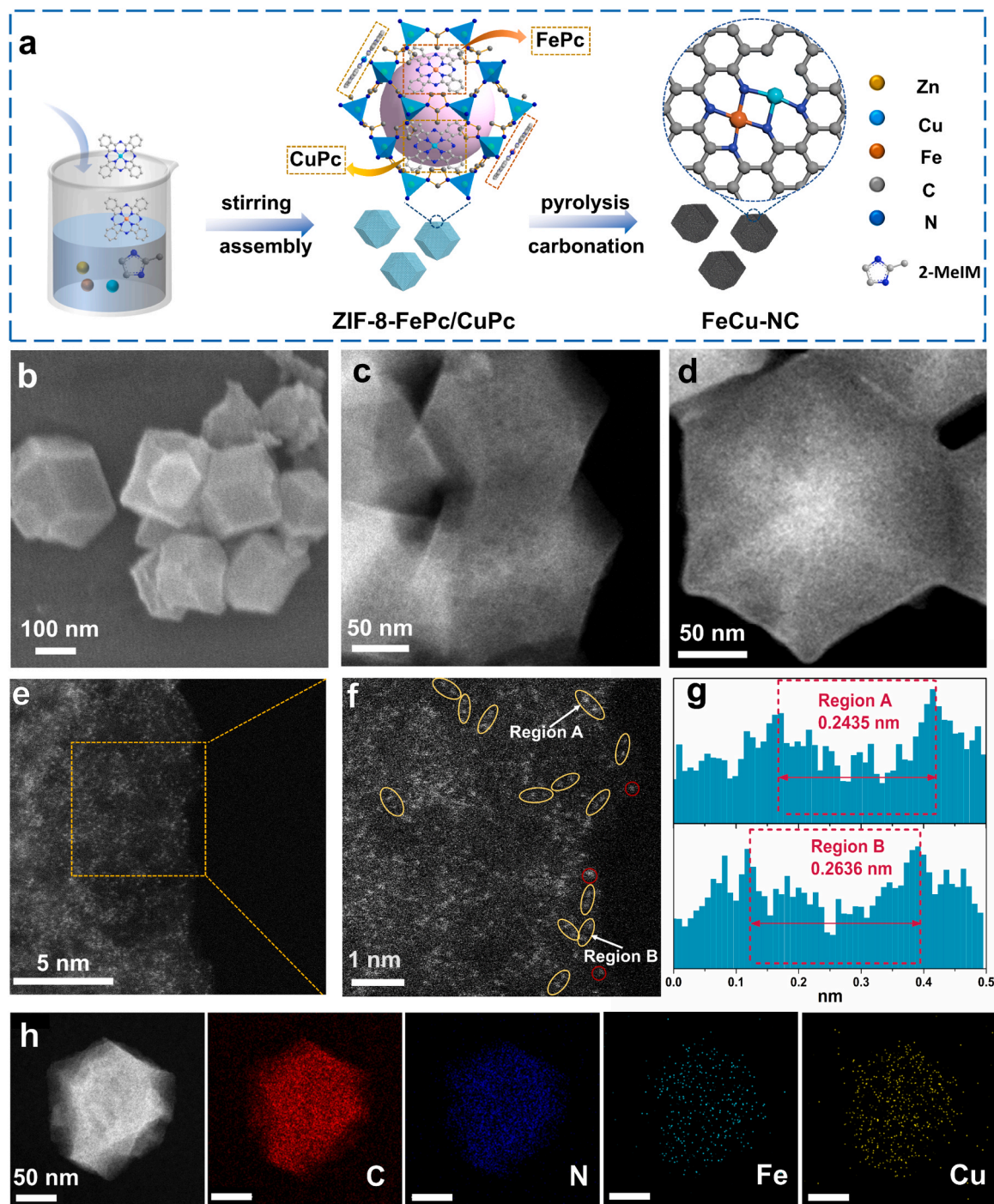

Fig. 1. (a) Schematic illustration of FeCu-NC synthesis strategy. (b) SEM, (c) TEM, (d) HRTEM, (e, f) HADDF-STEM images of FeCu-NC and the intensity profiles obtained for two metals corresponding to region A and B. And (h) the STEM with the related EDX images.

capacity and energy density as well as high charge-discharge cycling stability.

2. Results and discussion

2.1. Synthesis strategy and basic structural analysis for the FeCu-NC

Fig. 1a shows a schematic illustration of the pyrolysis process for synthesis of FeCu-NC by a facile one-pot strategy. The ZIF-8-FePc/CuPc precursor was obtained from the solution of $Zn(NO_3)_2 \cdot 6\ H_2O$, 2-MeIM, FePc and CuPc with methanol as the solvent at room temperature. As typical large conjugated and planar aromatic N_4-acrocylic complexes with D_{4h} symmetry [28], the FePc/CuPc molecules were captured on the ZIF-8 surface with π-π interaction, because the molecular sizes of FePc (14.6 Å) and CuPc (17.4 Å) are larger than that of the cavity diameter (11.6 Å) of ZIF-8 [29]. After the high temperature annealing treatments at about 950 ℃, the FePc/CuPc molecules decomposed, and some free Fe and Cu atoms were captured by the N-doped carbon skeletons from the pyrolysis of ZIF-8. Due to the spatial isolation effect of the FePc/CuPc phthalocyanine molecules and the strong coordination effect of nitrogen element, the Fe and Cu atoms were effectively isolated without the agglomeration of metal atoms. As shown in the scanning electron microscope (SEM) image (Fig. 1b), the FeCu-NC inherits the original dodecahedron morphology of ZIF-8 with an average size of about 200 nm. Similar phenomena were found for Fe-NC (Fig. S1) and Cu-NC (Fig. S2). No obvious particles were observed on the high-resolution transmission electron microscope (HRTEM) images of FeCu-NC (Fig. 1c and d). X-ray diffraction (XRD) patterns confirmed no change happens for the crystalline structure of ZIF-8 (Fig. S3) pre- and post-covering the FePc and CuPc molecules, and the ZIF-8-FePc/CuPc precursor totally transformed into amorphous FeCu-NC after the pyrolysis treatment. A broad diffraction peak at 24.1° and a weak one at 43.3° were observed for FeCu-NC, Fe-NC, Cu-NC and NC (Fig. S4), which are assigned to the (002) and (101) plans of graphitic carbon, respectively [30]. Raman spectra in Fig. S5 reflected the degrees of graphitization of FeCu-NC, Fe-NC, Cu-NC and NC. All the samples exhibited two bands with the peaks at 1350 cm^{-1} and 1590 cm^{-1}, due to the disordered sp^3 carbon (D-band) and graphitic sp^2 carbon (G-band), respectively [31]. The intensity ratio of the D-band and G-band for FeCu-NC (1.26) is a little higher than that of Fe-NC (1.23), indicating that introduction of Cu atoms in the carbonaceous framework leads to a bit more structural defects and/or lower degree of graphitization. N_2 adsorption-desorption isotherms demonstrated that the FeCu-NC, Fe-NC and Cu-NC have similar isotherms with the obvious type-H4 hysteresis loops [24], manifesting the existence of abundant micropores and mesopores. The Brunauer-Emmett-Teller (BET) specific surface area of FeCu-NC is 355.8 $m^2\ g^{-1}$ (Fig. S6) less than those of Fe-NC (508.1) and Cu-NC (545.7 $m^2\ g^{-1}$), because the Fe and Cu two elements co-anchored on the NC matrix where the presence of two different types of ions may possibly affect the breathing and flexibility of the porous structure [32]. The pore size distributions (Figs. S7 and S8) analysis indicated that the pore widths of the FeCu-NC, Fe-NC and Cu-NC catalysts are distributed in the range of 0.5–2.0 nm, which make for the effective mass transfer of the reactants in the ORR process [33]. High-angle annular dark-field scanning transmission electron microscope (HAADF-STEM) was used to further observe the metal atoms. Many bright dots in pairs on the atomic scale were observed on the carbonaceous hosts and the average distance between two bright dots in the 20 paired atoms was calculated to be approximately 2.5 Å (Fig. 1e-g), which favors the occurrence of coupling between the diatoms and regulation of the electronic structure around iron atoms. Energy dispersive X-ray (EDX) mapping analysis (Fig. 1h) showed that the C, N, Fe and Cu elements are evenly distributed in the carbon skeleton. Inductively coupled plasma optical emission spectrometry (ICP-OES) analysis (Table S1) exhibited that the contents of Fe and Cu are 1.11 wt% and 0.36 wt% for FeCu-NC, respectively.

X-ray photoelectron spectroscopy (XPS) spectrum manifested the atomic percentages of C (86.35 at%), N (8.84 at%), Fe (0.20 at%) and Cu (0.18 at%) elements in the resultant FeCu-NC. Similar contents of N and Fe/Cu were also found for Fe-NC and Cu-NC samples (Table S2). The deconvoluted characteristic peaks at 284.8, 285.6, 286.5 and 290.8 eV in the high-resolution C 1 s XPS spectra confirmed the existence of C-C, C-N, C-O and C═O (Figs. 2a and S9)[34]. The existence of C-N chemical bonds indicated that N atoms are successfully doped into the carbonaceous skeleton. Five deconvoluted characteristic peaks at 398.5, 399,9, 400.9, 401.5 and 402.8 eV could be found from the high-resolution N 1 s XPS spectra (Fig. 2b and S10), which correspond to pyridinic N, Fe/Cu-N, pyrrolic N, graphitic N and oxidized N, respectively [35,36]. The existence of Fe/Cu-N chemical bonds indicated that the Fe/Cu atoms are coordinated with the skeleton N in the carbon matrix. The deconvoluted characteristic peaks at 710.1/715.9, 721.6/726.1 eV could be found in the Fe 2p spectrum of Fe/Cu-NC (Fig. 2c), corresponding to the Fe^{2+}/Fe^{3+} of Fe $2p_{3/2}$ and Fe $2p_{1/2}$, respectively [37]. In the high-resolution Cu 2p spectrum of FeCu-NC, the peaks at 932.2/934.6 and 951.6/953.8 eV are assigned to Cu^+/Cu^{2+} of Cu $2p_{3/2}$ and Cu $2p_{1/2}$. The ratio of Cu^+/Cu^{2+} significantly increased in FeCu-NC (about 0.7/0.3) compared to that of Cu-NC (about 0.2/0.9), suggesting the decreased charge density around Cu sites for FeCu-NC. Interestingly, a red shift of approximate 0.6 eV and a blue shift of about 0.5 eV were observed for the binding energies of Fe 2p and Cu 2p peaks of FeCu-NC compared to that of Fe-NC and Cu-NC, respectively, due to the effective synergistic effect between Fe and Cu atoms.

2.2. Microstructure analysis for the atomically distributed metal species

X-ray absorption near-edge structure (XANES) and extended X-ray absorption fine structure (EXAFS) were used to further investigate the valence states and coordination environments of the metal atom centers. As shown in the Fe K-edge XANES (Fig. 3a), the absorption edge of FeCu-NC was located between the FePc and Fe_2O_3, indicating that the valence of Fe species is between +2 and +3. The average oxidation state of Fe in FeCu-NC is about +2.4 (Fig. 3b) derived from the first-derivative of XANES (Fig. S11a), which is lower than that of Fe-NC (+2.8). The decreased average oxidation state of Fe atoms is favorable to the desorption of oxygen intermediates based on the classical hard-soft-acid-base theory, which is conductive to accelerating the ORR process. Likewise, the absorption threshold of FeCu-NC in Cu K-edge XANES spectrum (Fig. 3c) was located between Cu_2O and CuO, indicating that the valence of Cu species in FeCu-NC is between +1 and +2. The relationship between near-edge absorption energy and oxidation state of Cu for the first order of XANES (Fig. S11b) indicated that the valence of Cu species in FeCu-NC is the mixture of Cu^+ and Cu^{2+}. Two strong peaks at 1.48 Å and 1.47 Å were presented in the Fourier transformed (FT) k^3-weighted extended X-ray absorption fine structure (FT-EXAFS) space spectra of Fe K-edge and Cu K-edge in FeCu-NC, respectively (Fig. 3d and e), corresponding to the Fe-N and Cu-N scattering paths. In addition, the predominant peaks for Fe-N and Cu-N bonds in FeCu-NC, Fe-NC and Cu-NC were shifted compared with those for FePc (1.51 Å) and CuPc (1.53 Å), as results of the different coordination environments from those of FePc/CuPc as well as interaction of atomic pairs between Fe and Cu. The EXAFS wavelet transforms (WT) (Fig. 3f) showed the scattering paths in R-space and K-space, and the maximum WT intensities of Fe K-edge in FeCu-NC and Fe-NC were at around 5.0 $Å^{-1}$ attributing to the Fe-N scattering paths. Meanwhile, the maximum WT intensity of Cu K-edge presented the Cu-N scattering paths of FeCu-NC and Cu-NC (around 5.8 $Å^{-1}$). The FT-EXAFS fitting (Fig. 3g and h) identified that the Cu atoms in FeCu-NC and Cu-NC are coordinated with three N atoms at 1.94 Å and the Fe atoms are coordinated with four N atoms at 1.97 Å (Table S3). Thus, the Fe and Cu species exist in the forms of FeN_4 and CuN_3 coordination environments in FeCu-NC. The structural reconstruction of CuPc driven by thermal energy may be responsible for the formation of CuN_3 single atomic sites [38,39]. It was previously indicated that the low N-coordination number of CuN_3 sites facilitated the
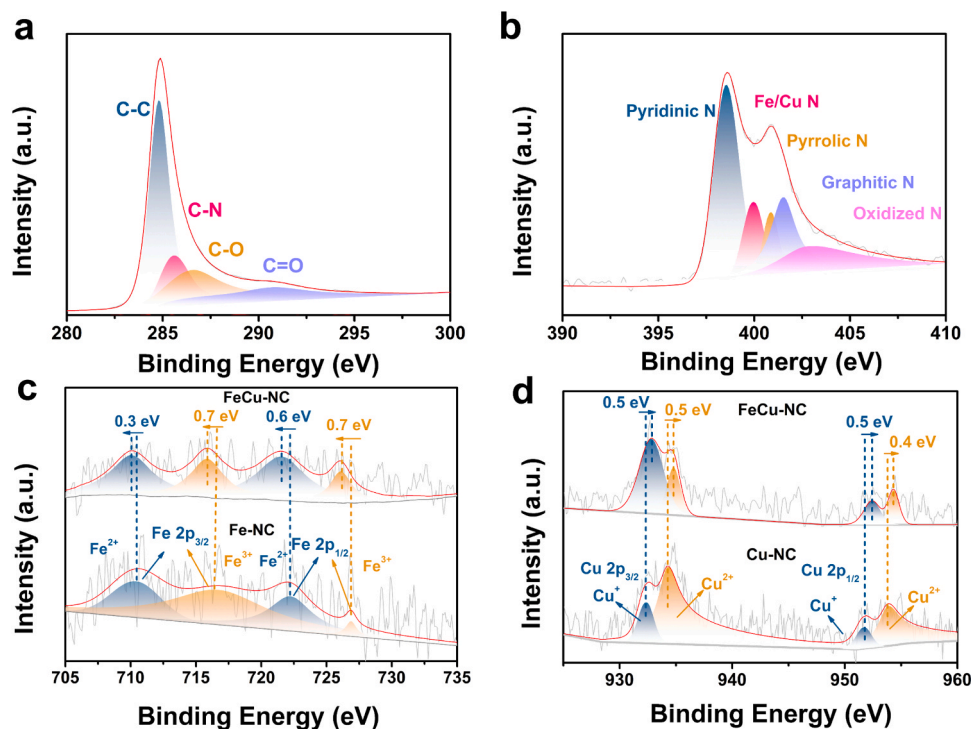
Fig. 2. XPS spectra of (a) N 1 s, (b) C 1 s of FeCu-NC, (c) Fe 2p of FeCu-NC and Fe-NC. And (d) Cu 2p of FeCu-NC and Cu-NC.

formation of O_2^* intermediates, thus promoting the ORR process [40]. Combining the average distance between Fe and Cu of about 2.5 Å and the optimized ORR electrocatalytic property, the structure model of FeCu-NC DAC with Fe(II,III)N$_2$(μ_2-N)$_2$Cu(I,II)N moieties can be obtained and given in Fig. 3g.

2.3. ORR electrocatalytic activity analysis for FeCu-NC

The ORR electrocatalysis activity of FeCu-NC was evaluated in O_2-saturated 0.1 M KOH alkaline medium based on the rotating ring-disk electrode (RRDE) measurements in a three-electrode system. The cyclic voltammetry (CV) curve of FeCu-NC showed a noticeable reduction peak potential at 0.88 V (Fig. S12), which is a little superior to that of the commercial Pt/C (0.87 V) and obviously better than that of Fe-NC (0.85 V). Meanwhile, the FeCu-NC presented the strongest cathodic current density of 1.42 mA cm^{-2}. Linear sweep voltammetry (LSV) was further conducted to obtain the ORR catalytic performance of the samples accurately (Fig. 4a). The results presented that FeCu-NC has the best ORR activity with the highest $E_{1/2}$ of 0.889 V, which is about 45, 36 and 125 mV higher than those of Pt/C (0.848 V), Fe-NC (0.863 V) and Cu-NC (0.764 V), respectively. And as shown in Fig. 4b, FeCu-NC displayed higher limiting current density (5.20 mA cm^{-2}) and kinetic current density (20.35 mA cm^{-2}@0.85 V), reflecting that the introduction of CuN$_3$ sites significantly improves the ORR catalytic activity and the mass transfer capacity [41]. The Tafel slope of 44.0 mV dec^{-1} was achieved over FeCu-NC which is clearly lower than that of the Pt/C (99.9 mV dec^{-1}), further evidencing the excellent reaction kinetics (Fig. 4c). Besides, the electrochemical active surface areas (ECSA) were estimated by the electrochemical double-layer capacitance (C_{dl}) in Fig. 4d, which were derived from the CV tests at different scan rates (Fig. S13). The calculation results showed that the ESCA of FeCu-NC (232 cm^2) is larger than that of Fe-NC (200 cm^2) and more than twice that of Cu-NC (83 cm^2), indicating that the FeCu-NC provides more electrocatalytic active sites for the ORR process.

The electron transfer number of the FeCu-NC was calculated by the Koutecky-Levich (K-L) plots derived from the LSV curves at various rotation speeds in Fig. 4e, and it was in the range of 3.78–3.86, similar to

those of Fe-NC and Pt/C (Fig. S14). As shown in Fig. 4f and S15, the RRDE tests further presented that the transfer electron number of FeCu-NC was 3.79–3.95 at the voltage range of 0.3–0.8 V, also similar to those of Fe-NC (3.72–3.92), Cu-NC (3.40–3.60) and Pt/C (3.88–3.91). The results manifested that FeCu-NC follows a 4e$^-$ pathway in the ORR process, which is consistent with the K-L plots. After 10,000 cycles of accelerated durability test (ADT), the $E_{1/2}$ of FeCu-NC had a slightly negligible decay (~2 mV), indicating that the FeCu-NC has a good stability for ORR over the long-term course (Fig. 4g). As shown in Fig. 4h, the current density retention of FeCu-NC presented no noticeable variation after the addition of 1 M methanol, but the current density retention of Pt/C turned sharply, which demonstrated the excellent methanol tolerance of FeCu-NC. In addition, Fig. 4i and Table S4 showed the excellent ORR activity and stability of FeCu-NC standing above the typical state-of-the-art related results [42–50].

2.4. Theory calculation on the structure model and electrocatalytic mechanism

To deeply understand the effect of CuN$_3$ moieties on the catalytic activity of FeN$_4$ sites, the first-principle DFT calculations were performed. As shown in Fig. S16, three models of FeCu-NC-I, FeCu-NC-II and FeCu-NC-III with the atomic distances between Fe and Cu at 2.44, 3.02 and 4.34 Å, respectively, were constructed for FeCu-NC based on the above HADDF-STEM, XANES and EXAFS analysis. The differential charge distributions (DCDs) were simulated for the FeCu-NC-I, FeCu-NC-II, FeCu-NC-III, Fe-NC and Cu-NC (Fig. S17). Small changes were found for DCDs among the FeCu-NC-I, FeCu-NC-II and FeCu-NC-III structures, while large differences of DCDs were observed among FeCu-NC, Fe-NC and Cu-NC. Furthermore, the electron density difference analysis showed that the electron density of Fe sites in FeCu-NC is higher than that of Fe sites in Fe-NC, suggesting that there are more low-valence Fe^{2+} ions in the FeN$_4$ moieties in consistence with the XANES analyses. The Gibbs free energy changes (ΔG) of Fe and Cu sites on Fe-NC, Cu-NC and FeCu-NC were calculated, respectively (Fig. 5a, b and Figs. S18-S20). The RDS of Fe-NC, Cu-NC, FeCu-NC-II and FeCu-NC-III is the last step of ORR, i.e., *OH reduction, mainly due to the excessive
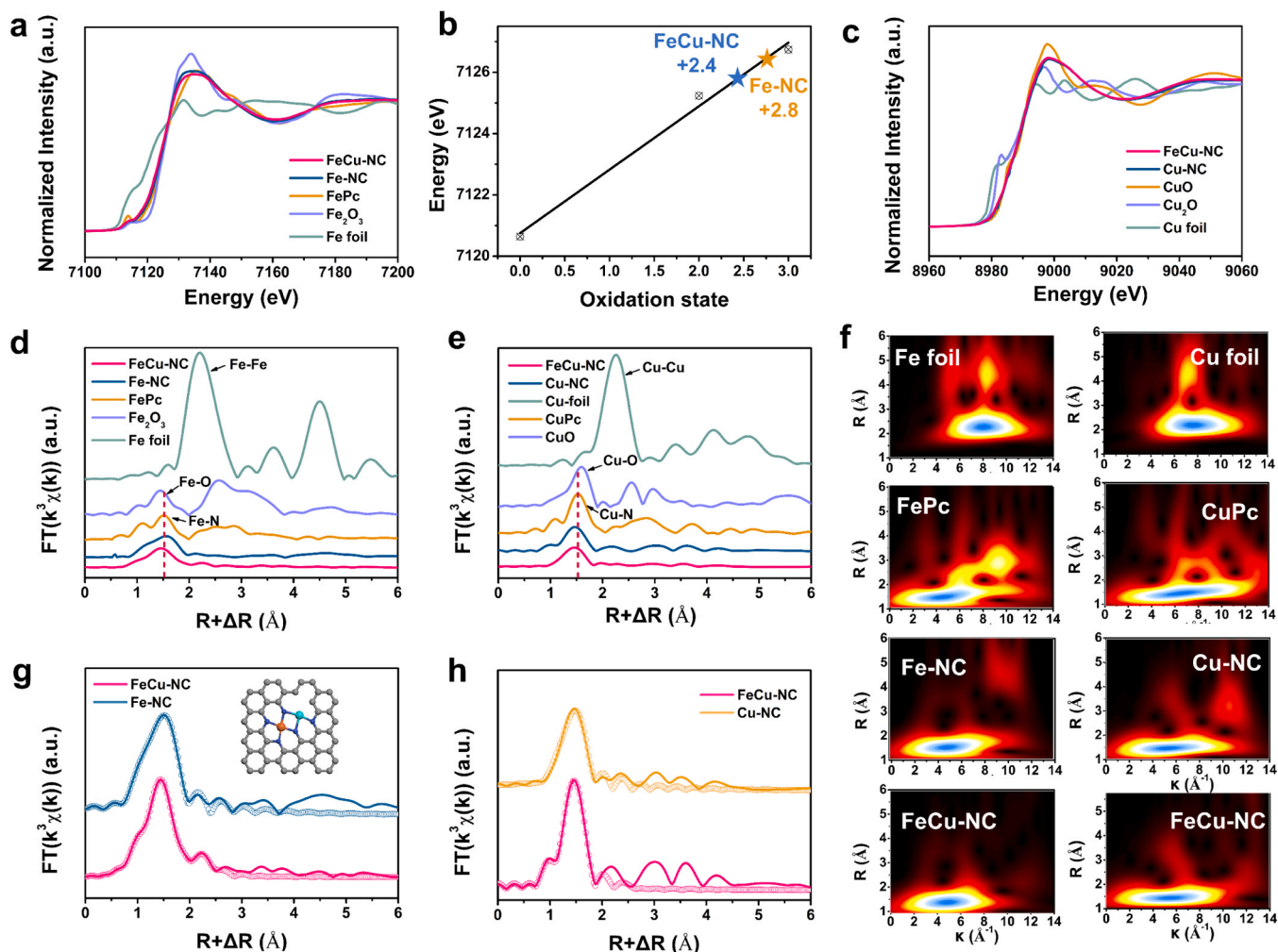
Fig. 3. (a) Fe K-edge XANES spectra. (b) Fitted oxidation state of the first-derivative Fe K-edge XANES spectra. (c) Cu K-edge XANES spectra. (d, e) FT-EXAFs of Fe K-edge for FeCu-NC, Fe-NC, FePc, Fe₂O₃, Fe foil, Cu-NC, CuPc, CuO and Cu foil, respectively. (f) Fe K-edge and Cu K-edge EXAFS WT images of FeCu-NC, Fe-NC, Cu-NC and the references. And (g, h) Fe K-edge and Cu K-edge EXAFS fitting curves.

adsorption ability of the active site with oxygen intermediates. However, the FeCu-NC-I with the closest atom distance between Fe and Cu has the lowest ΔG of 0.46 eV for the RDS from *O₂ to *OOH, indicating that FeCu-NC-I has an optimized four-electron ORR pathway with decreased dissociation energy of *OOH intermediate and better ORR activity. Besides, the catalyst with FeN₄ and CuN₄ bimetallic sites bridged by two nitrogen atoms presented the same RDS of *OH reduction as FeN₄[51], which is different with our FeCu-NC-I with the RDS from *O₂ to *OOH, presenting that the charge distribution around the FeN₄ active sites and ORR pathway are influenced by the coordination configuration and electronic structure of the neighboring Cu sites. As shown in Fig. 5c, the overpotential of FeCu-NC-I is closed to the Pt(111) catalyst for the four-electron reduction of O₂ according to the volcano plot, which presents the distinguished kinetics process of FeCu-NC-I [52]. The charge density values around Fe sites and Cu sites for FeCu-NC (Table S5) showed that the Cu sites have fewer charge density value than that of Fe sites. So, the Cu sites have a stronger binding energy for the oxygen intermediates possibly. The calculated ΔG of Cu sites on FeCu-NC was 2.00 eV (Fig. S21) for the RDS (*OH reduction), which is much higher than that of Cu-NC (1.11 eV) as well as those of Fe-NC and FeCu-NC, thus the possibility that CuN₃ moieties are the main active sites could be excluded. As a result, the Fe sites rather than Cu sites are the electrocatalytically active centers existed as FeCu-NC-I model in the structural framework of FeCu-NC.

Fig. 5d shows the optimized adsorption configurations of

intermediates on the FeCu-NC-I in the 4e⁻ ORR process. The charge transfer number between *OOH and FeCu-NC-I (0.409 e) was smaller than the other models (Fig. 5e and S22), which suggests fewer electrons flow from Fe sites to O atoms at FeCu-NC-I, resulting in the weaker interaction between *OOH and Fe sites. In addition, the Fe-O bond length of FeCu-NC-I (Fig. 5e and S23) was the longer (1.86 Å), corresponding to the weaker *OOH binding energy (0.46 eV). The density of state (DOS) of FeCu-NC was different from those of Fe-NC and Cu-NC (Fig. S24), where the calculated d-band center of Fe sites significantly negative shifted from −0.29 eV to −2.58 eV (Table S7) and FeCu-NC-I had a more positive adsorption energy (4.154 eV). All the above results suggest that the weaker interaction of oxygen intermediates on the Fe active center at FeCu-NC-I makes it easier for desorption of *OOH intermediates from the catalyst surface, which is intrinsically responsible for the excellent ORR activity of FeCu-NC. The structural stability of FeCu-NC was also evaluated (Fig. 5 f). The geometry of FeCu-NC-I had no obvious deformation when the temperature was increased to 1000 K and lasted for 10 ps, indicating its high thermodynamic stability. Thus, the synergistic effect of Fe-Cu dual atoms in FeCu-NC reduced the adsorption of the oxygen intermediate OOH* and optimized the four-electron ORR pathway, improving the electrochemical performance of ORR process.
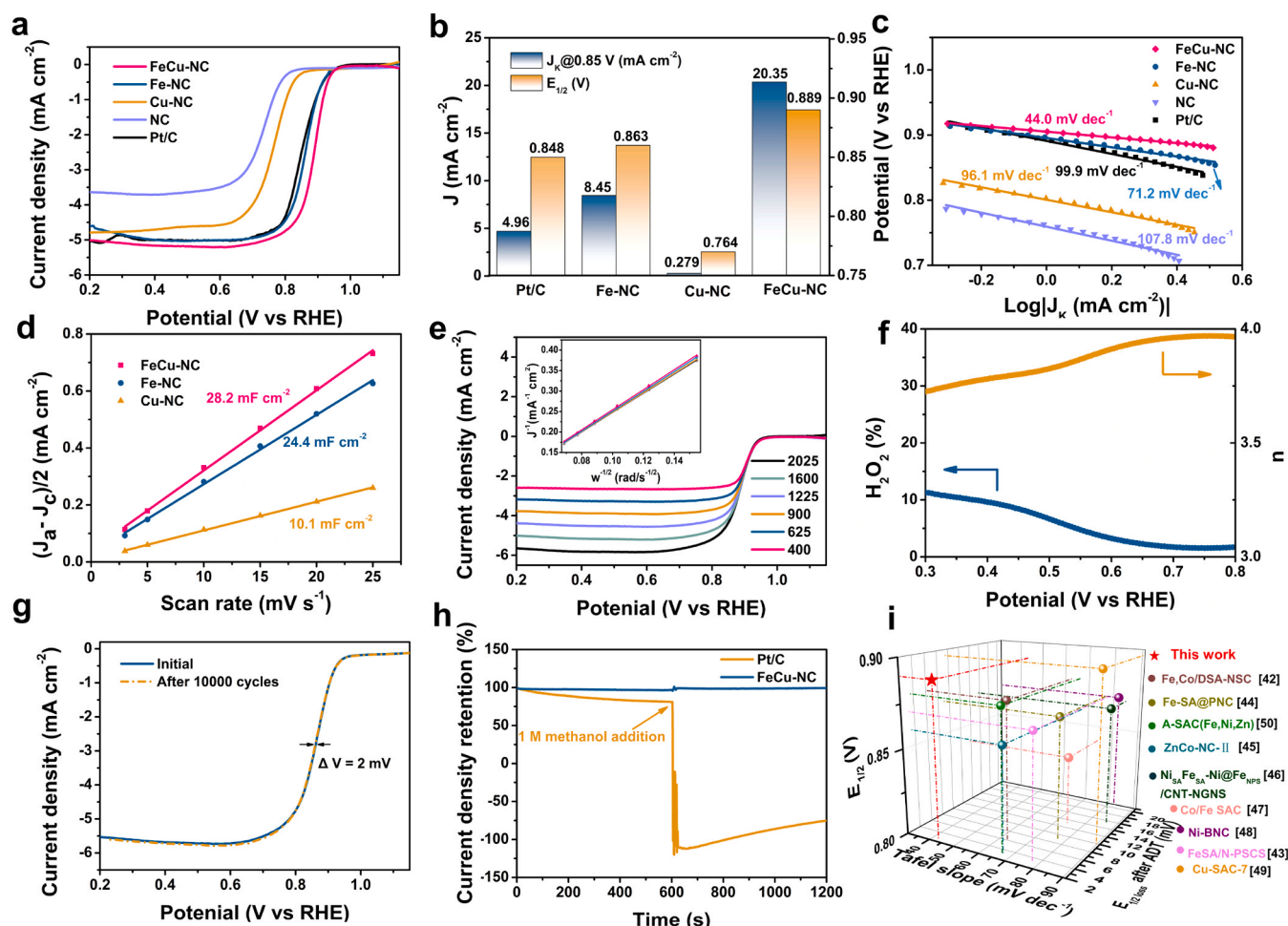
Fig. 4. (a) ORR polarization curves. (b) J_k at 0.85 V and half-wave potential, and (c) Tafel slopes of FeCu-NC, Fe-NC, Cu-NC, NC and 20% Pt/C in O_2 saturated 0.1 M KOH at 1600 rpm. (d) Current density at various scan rate in a non-Faradaic range for FeCu-NC, Fe-NC and Cu-NC. (e) LSV plots with the corresponding K-L plots. (f) H_2O_2 yields and electron transfer numbers. (g) LSV curves of FeCu-NC before and after 10,000 cycles. (h) Current density retentions of FeCu-NC and Pt/C with the addition of 1 M methanol. And (i) comparison of ORR performance, kinetics rate and stability for FeCu-NC and the reported results.

2.5. Zn-air battery performance analysis

Homemade Zn-air battery was assembled by using FeCu-NC as the air cathode and Zn foil as the anode to evaluate its application as rechargeable energy device. The FeCu-NC based cell exhibited an excellent maximum power density of 91.2 mW cm^{-2} (Fig. 6b), which is higher than that of the Pt/C based cell (82.8 mW cm^{-2}). The open-circuit voltage of the FeCu-NC based cell (1.47 V) was 20 mV higher than that of the Pt/C based cell (1.45 V) (Fig. 6c). Furthermore, the discharge specific capacity and energy density of the Zn-air battery were measured by the galvanostatic discharge at 10 mA cm^{-2}. As shown in Fig. 6d, the specific capacity and energy density of FeCu-NC based cell were calculated to be 795 mAh g^{-1} and 998 Wh kg^{-1}, respectively, which are higher than those of the Pt/C based cell (696 mAh g^{-1} and 875 Wh kg^{-1}). As a result, the utilization rate of Zn for FeCu-NC was up to 91.9%. After the galvanostatic discharge test, only a slight decrease of the power density was observed for the FeCu-NC based cell (Fig. S25). Fig. 6d provided the rate performance of FeCu-NC and Pt/C based cells. The voltages of FeCu-NC based cell are higher than those of the Pt/C based cell at different current densities.

The Zn-air battery was assembled using FeCu-NC + RuO$_2$ (1: 1) coated onto the nickel foam with gas layer as the air cathode for the galvanostatic discharge-charge test, and it was evaluated at a current density of 10 mA cm^{-2} with an interval of 10 min. Moreover, the FeCu-NC + RuO$_2$ based cell presented a stable charge/discharge potential at

10 mA cm^{-2} for 160 cycles (53 h), which is much better than that of the Pt/C + RuO$_2$ based cell. The SEM (Fig. S26) and XRD (Fig. S27) indicate that the FeCu-NC still maintained a uniform dodecahedral morphology with amorphous structure after the cycles. The property degradation of rechargeable Zn-air battery was caused by some oxidation of the Zn anode after the cycles based on the SEM (Fig. S89) and XRD (Fig. S29) analyses. The electrocatalytic oxygen evolution performance (OER) of FeCu-NC, Fe-NC, Cu-NC and RuO$_2$ were tested (Fig. S30), which exhibited the current density of 10 mA cm^{-2} at the overpotential of 407, 443, 456 and 363 mV, respectively. And the Tafel slope of 90.0 mV dec^{-1} was achieved over FeCu-NC. The excellent device performance is due to the synergistic effect of Fe-Cu dual atoms, which effectively improves the catalytic activity and cycling stability.

3. Conclusion

In summary, we have successfully prepared the single-atom Fe and Cu co-anchored on N-doped carbonaceous catalyst FeCu-NC by one-pot pyrolysis method using ZIF-8-FePc/CuPc as the precursor. The CuN$_3$ moieties can effectively change the charge distribution around the FeN$_4$ sites, leading to increased charge density of the FeN$_4$ sites. The weaker interaction between the FeN$_4$ site and *OOH intermediate results in an optimized four-electron reaction pathway, effectively improving the intrinsic activity of FeN$_4$ sites for ORR process. As a result, the FeCu-NC DAC exhibits an excellent ORR electrocatalytic activity superior to that
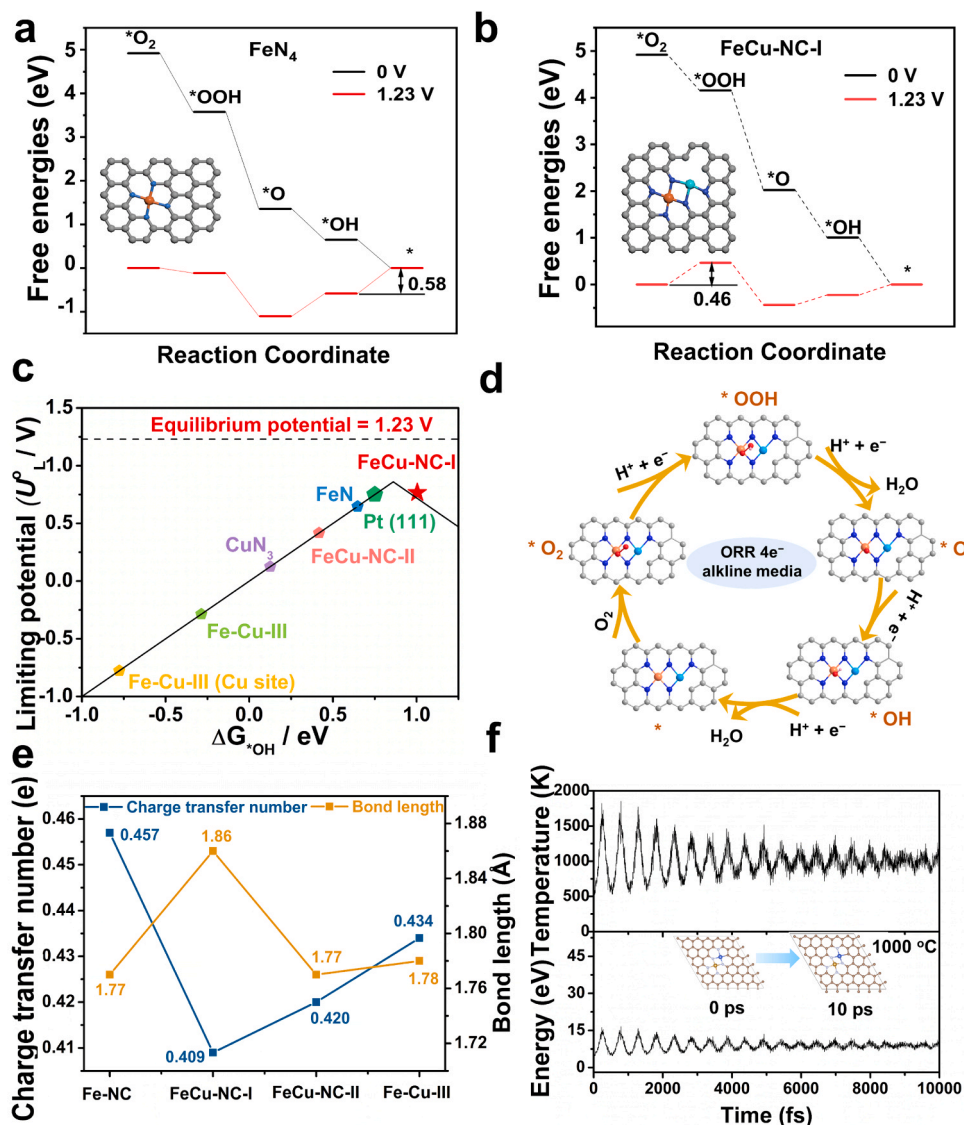
Fig. 5. (a, b) The Gibbs free energy diagram for $4e^-$ ORR process of Fe site on Fe-NC and FeCu-NC-I. (c) Theoretically calculated ORR volcano for $4e^-$ pathway. (d) The optimized adsorption configurations of intermediates in the ORR process. (e) Charge transfer number and Fe-O bond length of OOH* on FeCu-NC. And (f) variations of energy and temperature against the time of FeCu-NC-I, and insert are top views of the atomic configuration. The simulation is run under 1000 K for 10 ps.

of the commercial Pt/C. The structure-activity relationship of FeCu-NC for ORR process was clarified by the DFT calculation, XPS, XANES analysis and electrochemical test. Furthermore, the FeCu-NC has an outstanding cyclic and structural stability. The self-assembly Zn-air battery based on the FeCu-NC has a large specific capacity of 795 mAh g^{-1} and energy density of 998 Wh kg^{-1} as well as high charge-discharge cycling stability. The strategy of regulating the electronic structure of active centers may provide a valuable reference for the rational design and construction of advanced atomically distributed catalyst for oxygen reduction reaction.

4. Experimental

4.1. Chemical material

Potassium hydroxide (KOH), methanol (MeOH), Zn nitrate hexahydrate $Zn(NO_3)_2 \cdot 6\ H_2O$ (99%, AR), iron(II) phthalocyanine (FePc, >97%, AR), copper(II) phthalocyanine (CuPc, >90%, AR) and 2-methylimidazole (2-MeIM) were used without further purification. 20 wt% Pt/C

was obtained from Alfa Aesar. Deionized water was used without further purification.

4.2. Synthesis of the ZIF-8-FePc/CuPc precursor

Typically, the ZIF-8-FePc/CuPc precursor was prepared by the one-pot strategy [45]. 2.97 g $Zn(NO_3)_2 \cdot 6\ H_2O$, 50 mg FePc and 50 mg CuPc were dissolved in 80 mL of methanol. Next, 5.96 g 2-MeIM dissolved in 70 mL methanol was quickly added into the above solution and stirred at room temperature for 24 h. The dark blue product was collected by centrifugation and dried in vacuum oven at 70 ℃ for overnight. The synthesis procedures of ZIF-8-FePc, ZIF-8-CuPc and ZIF-8 were similar with that of ZIF-8-FePc/CuPc, except for the addition of CuPc and FePc separately.

4.3. Synthesis of FeCu-NC, Fe-NC, Cu-NC and NC

The ZIF-8-FePc/CuPc, Fe-ZIF-8, Cu-ZIF-8 and ZIF-8 were annealed at 950 ℃ for 3 h under the N_2 atmosphere to obtain the FeCu-NC, Fe-NC,
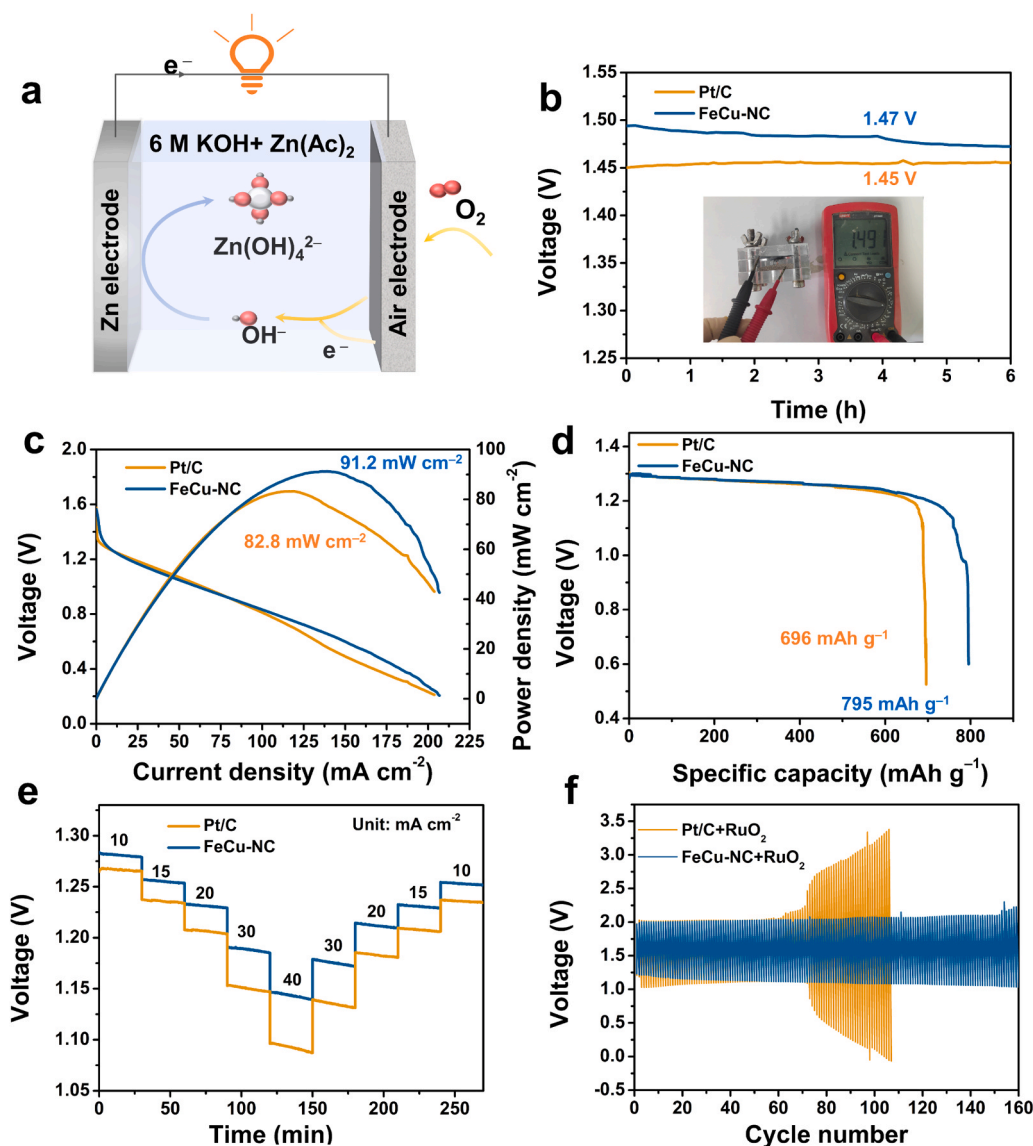
Fig. 6. (a) Schematic illustration of an as-assembled liquid Zn-air battery. And (b) open circuit potential, (c) polarization and power density curves, (d) galvanostatic discharge specific capacity at 10 mA cm^{-2}, (e) rate capabilities and (f) galvanostatic discharge-charge curves at 10 mA cm^{-2} of FeCu-NC compared with that of Pt/C.

Cu-NC and NC samples, respectively.

4.4. Characterization method

XRD patterns were carried out by D/MAX2200pc X-ray diffractometer (Rigaku, Japan) with Cu K$_\alpha$ radiation ($\lambda = 1.5418$ Å). SEM images were collected on a Quanta 250FEG. TEM images were determined on a Tecnai F20. The dark-field HRTEM images were acquired at an accelerating voltage of 200 kV (JEOL 2100 F). HAADF-STEM measurements with sub-angstrom resolution were observed through an aberration-corrected FEI Titan 80–300 scanning transmission electron microscope operating. EDX mapping analyses were obtained on the FEI Titan 80–300. XPS measurements were performed on a PHI Quantera II (Ulvac-Phi Inc., Japan). Raman spectra were collected on a LabRAM Aramis instrument (Horiba Jobin Yvon, France). ICP-OES analysis was carried out on an Agilent 725 ICP-OES. N$_2$ adsorption-desorption isotherms were acquired using a Micromeritics ASAP 2010 analyzer at 77 K. X-ray absorption fine structure spectra (Fe K-edge and Cu K-edge) were collected at a 1W1B station in Beijing Synchrotron Radiation Facility (BSRF).

4.5. Electrochemical measurement

All electrochemical measurements were performed on a standard three-electrode system on a Wavedriver 20 electrochemical workstation (PINE Instrument Company) at 25 ℃. The catalysts-loaded RRDE (0.247 cm^2) were used as the work electrode. The graphitic carbon, Hg/HgO electrode (filled with 1 M KOH) and 0.1 M KOH were used as the counter electrode, reference electrode and electrolyte, respectively. All measured potentials given in the paper were converted into the reversible hydrogen electrode (RHE) scale by the formula: $E_{RHE} = E_{SCE} + 0.059*pH + 0.098$. To prepare the uniform catalysts ink, 5 mg of the electrocatalyst powder was dispersed into a mixture of 240 μL ethanol, 240 μL deionized water and 20 μL Nafion solution under ultrasonication until the solution uniform dispersion. Dropping 10 μL of the above catalyst ink on the surface of glassy carbon electrode (GCE) with the catalyst loading of about 0.4 mg cm^{-2}. The loading of commercial Pt/C (20 wt%, Alfa Aesar, UK) and RuO$_2$ were ~0.2 mg cm^{-2}. CV and LSV measurements of ORR were collected at 10 mV s^{-1} within the range from 0 to 1.2 V (vs RHE, the same below) in an O$_2$ or N$_2$ saturated 0.1 M KOH solution. LSV measurements of OER were collected at 5 mV s^{-1} within the range from 1.2 to 1.9 V in an O$_2$ saturated 0.1 M KOH

solution. The RRDE was measured to determine 4e⁻ selectivity, the peroxide yield (HO_2^- %) and the transfer electron number (n). The ring potential of RRDE measurement was 1.5 V (vs RHE). The durability test was investigated via the ADT after 10,000 cycles of CV tests within the range from 0.62 to 1.12 V (vs RHE), and the LSV curves were compared before and after the ADT. The potentials are all relative to the reversible hydrogen electrode. The current density data are presented with *iR* correction.

4.6. Zn-air battery test

For assembling a homemade Zn-air battery, the polished Zn plate with a thickness of 0.5 mm and air electrode were employed as the anode and cathode, respectively. The air electrode was prepared with commercial carbon paper loading active materials. And the mixture of 6 M KOH and 0.2 M $Zn(OAC)_2$ as aqueous electrolyte. The gas diffusion layer (GDL) was prepared as follows: FeCu-NC (10 mg) and Nafion solution (5 wt%, 100 μL) were dispersed in mixture of 450 μL ethanol and 450 μL deionized water. The catalyst ink was uniformly dropped onto the carbon paper with a mass loading of ~1 mg cm⁻² and dried at 60 ℃ overnight. Polarization curve and open-circuit potential (OCP) were collected at 5 mV s⁻¹ on the Wavedriver electrochemical workstation. The galvanostatic discharge test and galvanostatic discharge-charge curve were carried out at 10 mA cm⁻² on an Arbin testing system. The rechargeable Zn-air battery was fabricated using the same protocol as that of primary battery and determined at a current density of 10 mA cm⁻² with an interval of 10 min (discharge for 10 min, charge for 10 min) under room temperature (Arbin Instruments).

CRediT authorship contribution statement

Qiuming Gao: Writing – review & editing, Supervision, Resources, Project administration, Methodology, Investigation, Funding acquisition, Formal analysis, Conceptualization. **Lilong Zhang:** Methodology, Investigation, Formal analysis. **Xiao Liang:** Formal analysis. **Hong Xiao:** Formal analysis. **Huifeng Zhuang:** Formal analysis. **Fanchao Zhang:** Formal analysis. **Tengfei Zhang:** Formal analysis. **Pinyu Han:** Formal analysis. **Wenjing Dai:** Formal analysis. **Fan Gao:** Formal analysis. **Jian Zhang:** Software, Methodology, Formal analysis. **Lirong Zheng:** Software, Methodology, Formal analysis. **Mengyuan Xu:** Writing – original draft, Methodology, Investigation, Formal analysis.

Declaration of Competing Interest

The authors declare that they have no known competing financial interests or personal relationships that could have appeared to influence the work reported in this paper.

Data availability

Data will be made available on request.

Acknowledgements

Appendix A. Supporting information

Supplementary data associated with this article can be found in the online version at doi:10.1016/j.apcatb.2024.123866.

References

[1] Q.F. Liu, Z.F. Pan, E.D. Wang, L. An, G.Q. Sun, Aqueous metal-air batteries: fundamentals and applications, Energy Storage Mater. 27 (2020) 478–505.

[2] H.J. Huang, D.S. Yu, F. Hu, S.C. Huang, J.N. Song, H.Y. Chen, L.L. Li, S.J. Peng, Clusters induced electron redistribution to tune oxygen reduction activity of transition metal single-atom for metal-air batteries, Angew. Chem. Int. Ed. 61 (2022) e202116068.

[3] S. Zaman, L. Huang, A.I. Douka, H. Yang, B. You, B.Y. Xia, Oxygen reduction electrocatalysts toward practical fuel cells: progress and perspectives, Angew. Chem. Int. Ed. 60 (2021) 17832–17852.

[4] D. Yang, H.T. Tan, X.H. Rui, Y. Yu, Electrode materials for rechargeable zinc-ion and zinc-air batteries: current status and future perspectives, Electrochem. Energy Rev. 2 (2019) 395–427.

[5] J.Y. Zhao, J. Lian, Z.X. Zhao, X.M. Wang, J.J. Zhang, A review of in-situ techniques for probing active sites and mechanisms of electrocatalytic oxygen reduction reactions, Nano Micro Lett. 15 (2023) 19.

[6] L. Xu, S.Q. Wu, X.Y. He, H. Wang, D.J. Deng, J.C. Wu, H.N. Li, Interface engineering of anti-perovskite Ni_3FeN/VN heterostructure for high-performance rechargeable zinc-air batteries, Chem. Eng. J. 437 (2022) 135291.

[7] C.X. Zhao, J.N. Liu, J. Wang, D. Ren, J. Yu, X. Chen, B.Q. Li, Q. Zhang, A delta E=0.63 V bifunctional oxygen electrocatalyst enables high-rate and long-cycling zinc-air batteries, Adv. Mater. 33 (2021) 2008606.

[8] X.Q. Wang, Z.J. Li, Y.T. Qu, T.W. Yuan, W.Y. Wang, Y. Wu, Y.D. Li, Review of metal catalysts for oxygen reduction reaction: from nanoscale engineering to atomic design, Chem 5 (2019) 1486–1511.

[9] J. Wang, Y. Gao, H. Kong, J. Kim, S. Choi, F. Ciucci, Y. Hao, S.H. Yang, Z.P. Shao, J. Lim, Non-precious-metal catalysts for alkaline water electrolysis: operando characterizations, theoretical calculations, and recent advances, Chem. Soc. Rev. 49 (2020) 9154–9196.

[10] D.J. Deng, J.C. Qian, X.Z. Liu, H.P. Li, D. Su, H.N. Li, H.M. Li, L. Xu, Non-covalent interaction of atomically dispersed Cu and Zn pair sites for efficient oxygen reduction reaction, Adv. Funct. Mater. 32 (2022) 2203471.

[11] L.C. Liu, A. Corma, Metal catalysts for heterogeneous catalysis: from single atoms to nanoclusters and nanoparticles, Chem. Rev. 118 (2018) 4981–5079.

[12] S.K. Kaiser, Z.P. Chen, D.F. Akl, S. Mitchell, J. Perez-Ramirez, Single-atom catalysts across the periodic table, Chem. Rev. 120 (2020) 11703–11809.

[13] C. Gao, J.X. Low, R. Long, T.T. Kong, J.F. Zhu, Y.J. Xiong, Heterogeneous single-atom photocatalysts: fundamentals and applications, Chem. Rev. 120 (2020) 12175–12216.

[14] A. Kumar, S. Ibraheem, T.A. Nguyen, R.K. Gupta, T. Maiyalagan, G. Yasin, Molecular-MN4 vs atomically dispersed M-N-4-C electrocatalysts for oxygen reduction reaction, Coord. Chem. Rev. 446 (2021) 214122.

[15] H. Xu, D. Wang, P.X. Yang, A.M. Liu, R.P. Li, Y. Li, L.H. Xiao, X.F. Ren, J.Q. Zhang, M.Z. An, Atomically dispersed M-N-C catalysts for the oxygen reduction reaction, J. Mater. Chem. A 8 (2020) 23187–23201.

[16] C.X. Zhao, J.N. Liu, J. Wang, C.D. Wang, X. Guo, X.Y. Li, X. Chen, L. Song, B.Q. Li, Q. Zhang, A clicking confinement strategy to fabricate transition metal single-atom sites for bifunctional oxygen electrocatalysis, Sci. Adv. 8 (2022) eabn5091.

[17] M. Zheng, J. Wang, Regulating the oxygen affinity of single atom catalysts by dual-atom design for enhanced oxygen reduction reaction activity, Chem. Res. Chin. Univ. 38 (2022) 1275–1281.

[18] J.K. Norskov, J. Rossmeisl, A. Logadottir, L. Lindqvist, J.R. Kitchin, T. Bligaard, H. Jonsson, Origin of the overpotential for oxygen reduction at a fuel-cell cathode, J. Phys. Chem. B 108 (2004) 17886–17892.

[19] R.G. Wang, L.F. Zhang, J.Q. Shan, Y.Y. Yang, F. Lee, T.Y. Chen, J. Mao, Y. Zhao, L. J. Yang, Z.P. Hu, T. Ling, Tuning Fe spin moment in Fe-N-C catalysts to climb the activity volcano via a local geometric distortion strategy, Adv. Sci. 9 (2022) 2203917.

[20] H.X. Xu, D.J. Cheng, D.P. Cao, X.C. Zeng, A universal principle for a rational design of single-atom electrocatalysts, Nat. Catal. 1 (2018) 339–348.

[21] D. Wang, H. Xu, P.X. Yang, X.Y. Lu, J.Y. Ma, R.P. Li, L.H. Xiao, J.Q. Zhang, M.Z. An, Fe-N_4 and Co-N_4 dual sites for boosting oxygen electroreduction in Zn-air batteries, J. Mater. Chem. A 9 (2021) 13678–13687.

[22] B. Wang, J. Tang, X.H. Zhang, M. Hong, H.K. Yang, X. Guo, S. Xue, C.C. Du, Z. X. Liu, J.H. Chen, Nitrogen doped porous carbon polyhedral supported Fe and Ni dual-metal single-atomic catalysts: template-free and metal ligand-free sysnthesis with microwave-assistance and d-band center modulating for boosted ORR catalysis in zinc-air batteries, Chem. Eng. J. 437 (2022) 135295.

[23] T.T. Cui, Y.P. Wang, T. Ye, J. Wu, Z.Q. Chen, J. Li, Y.P. Lei, D.S. Wang, Y.D. Li, Engineering dual single-atom sites on 2D ultrathin N-doped carbon nanosheets attaining ultra-low-temperature zinc-air battery, Angew. Chem. Int. Ed. 61 (2022) e202115219.

[24] Y.T. He, X.X. Yang, Y.S. Li, L.T. Liu, S.W. Guo, C.Y. Shu, F. Liu, Y.N. Liu, Q. Tan, G. Wu, Atomically dispersed Fe-Co dual metal sites as bifunctional oxygen electrocatalysts for rechargeable and flexible Zn-air batteries, ACS Catal. 12 (2022) 1216–1227.

[25] A. Bhagi-Damodaran, M.A. Michael, Q.H. Zhu, J. Reed, B.A. Sandoval, E.N. Mirts, S. Chakraborty, P. Moenne-Loccoz, Y. Zhang, Y. Lu, Why copper is preferred over iron for oxygen activation and reduction in haem-copper oxidases, Nat. Chem. 9 (2017) 257–263.

[26] W.J. Fan, Z.L. Li, C.H. You, X. Zong, X.L. Tian, S. Miao, T. Shu, C. Li, S.J. Liao, Binary Fe, Cu-doped bamboo-like carbon nanotubes as efficient catalyst for the oxygen reduction reaction, Nano Energy 37 (2017) 187–194.

[27] Z.Y. Xiao, P.P. Sun, Z.L. Qiao, K.W. Qiao, H.X. Xu, S.T. Wang, D.P. Cao, Atomically dispersed Fe-Cu dual-site catalysts synergistically boosting oxygen reduction for hydrogen fuel cells, Chem. Eng. J. 446 (2022) 137112.

[28] A. Kumar, K. Sun, X.X. Duan, S.B. Tian, X.M. Sun, Construction of dual-atom Fe via face-to-face assembly of molecular phthalocyanine for superior oxygen reduction reaction, Chem. Mater. 34 (2022) 5598–5606.

[29] R. Jiang, L. Li, T. Sheng, G.F. Hu, Y.G. Chen, L.Y. Wang, Edge-site engineering of atomically dispersed Fe-N$_4$ by selective C-N bond cleavage for enhanced oxygen reduction reaction activities, J. Am. Chem. Soc. 140 (2018) 11594–11598.

[30] D.J. Deng, H.H. Zhang, J.C. Wu, X. Tang, M. Ling, S.H. Dong, L. Xu, H.A. Li, H. M. Li, Electronic structure and spin state regulation of vanadium nitride via a sulfur doping strategy toward flexible zinc-air batteries, J. Energy Chem. 89 (2024) 239–249.

[31] H. Wang, L. Xu, D.J. Deng, X.Z. Liu, H.A. Li, D. Su, Regulated electronic structure and improved electrocatalytic performances of S-doped FeWO$_4$ for rechargeable zinc-air batteries, J. Energy Chem. 76 (2023) 359–367.

[32] L.-A. Luis, L.-C. Javier, E.-R. María, O. Enrique, C. Joaquín, A.H.H. Bas, S. Michele, C.W. Joao͂, J.C.V. Bruno, M.E. Guillermo, Implementing mesoporosity in zeolitic imidazolate frameworks through clip-off chemistry in heterometallic iron-zinc ZIF-8, J. Am, in: Chem. Soc, 145, 2023, 3c08017.

[33] Z.Q. Zhang, Y.G. Chen, L.Q. Zhou, C. Chen, Z. Han, B.S. Zhang, Q. Wu, L.J. Yang, L. Y. Du, Y.F. Bu, P. Wang, X.Z. Wang, H. Yang, Z. Hu, The simplest construction of single-site catalysts by the synergism of micropore trapping and nitrogen anchoring, Nat. Commun. 10 (2019) 1657.

[34] L.C. Bai, C.S. Hsu, D.T.L. Alexander, H.M. Chen, X.L. Hu, A cobalt-iron double-atom catalyst for the oxygen evolution reaction, J. Am. Chem. Soc. 141 (2019) 14190–14199.

[35] Y.O. Ma, H.Y. Fan, C. Wu, M.D. Zhang, J.H. Yu, L. Song, K.R. Li, J.P. He, An efficient dual-metal single-atom catalyst for bifunctional catalysis in zinc-air batteries, Carbon 185 (2021) 526–535.

[36] Z. Wang, X.Y. Jin, C. Zhu, Y.P. Liu, H. Tan, R.Q. Ku, Y.Q. Zhang, L.J. Zhou, Z. Liu, S.J. Hwang, H.J. Fan, Atomically dispersed Co$_2$-N$_6$ and Fe-N$_4$ costructures boost oxygen reduction reaction in both alkaline and acidic media, Adv. Mater. 33 (2021) 2104718.

[37] Y.Y. Wang, A. Kumar, M. Ma, Y. Jia, Y. Wang, Y. Zhang, G.X. Zhang, X.M. Sun, Z. F. Yan, Hierarchical peony-like FeCo-NC with conductive network and highly active sites as efficient electrocatalyst for rechargeable Zn-air battery, Nano Res 13 (2020) 1090–1099.

[38] G.Y. Xing, M.M. Tong, P. Yu, L. Wang, G.Y. Zhang, C.G. Tian, H.G. Fu, Reconstruction of highly dense Cu-N$_4$ active sites in electrocatalytic oxygen reduction characterized by operando synchrotron radiation, Angew. Chem. Int. Ed. 61 (2023) e202211098.

[39] W.J. Wei, F.H. Lu, L.X. Cui, Y. Zhang, Y.Z. Wei, L.B. Zong, S heteroatom doping in highly porous carbonaceous spheres for boosted oxygen reduction reaction of atomically dispersed Fe-N-4 active sites, Carbon 197 (2022) 112–119.

[40] M.X. Shen, J. Liu, J. Li, C. Duan, C.Y. Xiong, W. Zhao, L. Dai, Q.Y. Wang, H. Yang, Y.H. Ni, Breaking the N-limitation with N-enriched porous submicron carbon spheres anchored Fe single-atom catalyst for superior oxygen reduction reaction and Zn-air batteries, Energy Storage Mater. 59 (2023) 102790.

[41] M.X. Shen, J.L. Qi, K. Gao, C. Duan, J. Liu, Q.Q. Liu, H. Yang, Y.H. Ni, Chemical vapor deposition strategy for inserting atomic FeN$_4$ sites into 3D porous honeycomb carbon aerogels as oxygen reduction reaction catalysts in high-performance Zn-air batteries, Chem. Eng. J. 464 (2023) 142719.

[42] H.Y.S. Lee, S.Y. Lee, High metal loaded Cu(i)N3 single-atom catalysts: superior methane conversion activity and selectivity under mild conditions, J. Mater. Chem. A 11 (2023) 15691–15701.

[43] S.H. Ma, Z. Han, K.Y. Leng, X.J. Liu, Y. Wang, Y.T. Qu, J.B. Bai, Ionic exchange of metal-organic frameworks for constructing unsaturated copper single-atom catalysts for boosting oxygen reduction reaction, Small 16 (2020) 2001384.

[44] K. Song, Y. Feng, X. Zhou, T. Qin, X. Zou, Y. Qi, Z. Chen, J. Rao, Z. Wang, N. Yue, X. Ge, W. Zhang, W. Zheng, Exploiting the trade-offs of electron transfer in MOF-derived single Zn/Co atomic couples for performance-enhanced zinc-air battery, Appl. Catal. B-Environ. 316 (2022) 121591.

[45] T.H. Nguyen, P.K.L. Tran, D.T. Tran, T.N. Pham, N.H. Kim, J.H. Lee, Single (Ni, Fe) atoms and ultrasmall core@shell Ni@Fe nanostructures dual-implanted CNTs-graphene nanonetworks for robust Zn- and Al-air batteries, Chem. Eng. J. 440 (2022) 135781.

[46] B. Liu, S. Wang, R. Feng, Y. Ni, F. Song, Q. Liu, Anchoring bimetal single atoms and alloys on N-doping-carbon nanofiber networks for an efficient oxygen reduction reaction and zinc-air batteries, ACS Appl. Mater. Interfaces 14 (2022) 38739–38749.

[47] F. Wang, R. Zhang, Y. Zhang, Y. Li, J. Zhang, W. Yuan, H. Liu, F. Wang, H.L. Xin, Modulating electronic structure of atomically dispersed nickel sites through boron and nitrogen dual coordination boosts oxygen reduction, Adv. Funct. Mater. 33 (2023) 2213863.

[48] X.Y. Yao, Y.Q. Zhu, T.Y. Xia, Z.L. Han, C.L. Du, L.F. Yang, J.C. Tian, X.L. Ma, J. H. Hou, C.B. Cao, Tuning carbon defect in copper single-atom catalysts for efficient oxygen reduction, Small 19 (2023) 2301075.

[49] J.-E. Tsai, W.-X. Hong, H. Pourzolfaghar, W.-H. Wang, Y.-Y. Li, A. Fe-Ni-Zn, triple single-atom catalyst for efficient oxygen reduction and oxygen evolution reaction in rechargeable Zn-air batteries, Chem. Eng. J. 460 (2023) 141868.

[50] J. Wang, C.X. Zhao, J.N. Liu, Y.W. Song, J.Q. Huang, B.Q. Li, Dual-atom catalysts for oxygen electrocatalysis, Nano Energy 104 (2022) 107927.

[51] H. Liu, L. Jiang, Y. Wang, X. Wang, J. Khan, Y. Zhu, J. Xiao, L. Li, L. Han, Boosting oxygen reduction with coexistence of single-atomic Fe and Cu sites decorated nitrogen-doped porous carbon, Chem. Eng. J. 452 (2023) 138938.

[52] J. Rossmeisl, G.S. Karlberg, T. Jaramillo, J.K. Norskov, Steady state oxygen reduction and cyclic voltammetry, Faraday Discuss. 140 (2008) 337–346.